Non-intrusive measurement of complex free surfaces using Laser Induced Fluorescence and stereo imaging

van Meerkerk, Mike; Poelma, Christian; Westerweel, Jerry

Publication date
2018

Document Version
Final published version

Published in
Proceedings of the 19th International Symposium on Application of Laser and Imaging Techniques to Fluid Mechanics

Citation (APA)
van Meerkerk, M., Poelma, C., & Westerweel, J. (2018). Non-intrusive measurement of complex free surfaces using Laser Induced Fluorescence and stereo imaging. In *Proceedings of the 19th International Symposium on Application of Laser and Imaging Techniques to Fluid Mechanics* (pp. 821-832). Instituto Superior Técnico.

Non-intrusive measurement of complex free surfaces using Laser Induced Fluorescence and stereo imaging

Mike van Meerkerk[1,*], C. Poelma[1], J. Westerweel[1]
1: Dept. of Process and Energy, Delft University of Technology, The Netherlands
* Correspondent author: M.vanMeerkerk@tudelft.nl

Keywords: free surface measurement, surface gravity waves, wave breaking

ABSTRACT

A quasi three-dimensional stereo-camera measurement technique has been devised that is able to measure liquid free surface profiles, by scanning a light sheet. The technique will be applied to study the variability of impact pressure observed during wave impact in a newly developed experimental set-up. The set-up imposes severe optical (single window) and accessibility (autoclave) constraints. The devised measurement technique is required to measure liquid free surface profiles over a domain of $(X, Y, Z) = (100, 100, 100)$ mm domain with an accuracy of 1 mm. The performance of the devised measurement technique is evaluated using a convential side-view measurement (Buckley et al 2017) in the water tunnel of the Laboratory for Aero- and Hydrodynamics at the Delft University of Technology. A free surface profile is generated by flow over a bump geometry (Gui et al 2014), which provides a repeatable and increasingly complex free surface profile. The free surface profile is determined for three different cases over a domain of $(X, Y, Z) = (170, 100, 62)$ mm with an averaged systematic error of 2.7 ± 1.2 mm. The observed error is systematic and implies that the edge detection procedure is not robust enough. In future work the systems measurement frequency and edge detection procedure will be improved.

1. Introduction

The dynamic behavior of waves remains an active research subject. The extreme pressures observed during a wave impact are a key feature for engineering applications. These wave impacts are observed for different wave types and length scales, e.g. large scale ocean waves (Blackmore & Hewson 1984) and laboratory-scale waves that are either sloshing (Lugni et al 2010, Lugni et al 2010) or single impact waves (Bullock et al 2007, Bagnold 1939, Chan and Melville 1988). Another striking feature of impacting waves is the large variability of impact pressures that is observed for ostensibly identical, scaled initial conditions.

This variability is often attributed to the geometry of the wave shape (Bredmose et al 2015), which defines the relative size of the air cushion before wave impact (Bagnold 1939), the impact coefficient (variability in impact velocity) (Song et al 2013) and the possibility of wave focusing (Peregrine 2003). However, measurements of impacting waves are often performed over singles

planes or points, limiting our understanding of the variability. This work introduces a method to measure the shape of a complex liquid free surface, in preparation of future studies on the variability of wave impact.

2. Surface measurement

In fluid mechanics, surface measurement techniques are used to study various interesting phenomena. The measurement of surface elevation and slope in time and space is challenging and often intrusive measurement devices, e.g. wave probes, are used. In recent years several optical techniques were developed to measure surface elevation and/or slope instantaneously and non-intrusively. However, optical measurement are limited by their physical working principle and/or required distinguishable patterns. To image a free surface in laboratory conditions, where the water is generally cleaner and the surface smoother compared to environmental applications, it is required to add either seeding or a fluorescent dye (Gomit et al. 2013).

The different measurement techniques can be grouped according to their working principle, as methods based on: (i) image correlation of textures (Wanek and Wu 2006; Zavadsky et al 2017); (ii) projection of a regular or irregular pattern (Andre and Bardet 2014; Buckley et al 2017; Gomit et al 2015; Wang et al 2018); and (iii) properties of light, such as reflection or refraction (Gomit et al 2013; Moisy et al 2009; Savelsberg et al 2006). Methods based on image correlation of textures can be troublesome in laboratory applications, as specular reflections and occlusions may result in low correlation values (Wanek and Wu 2006; Zavadsky et al 2017). The addition of seeding particles can resolve issues related to specular reflections (Turney et al 2009). However, the accumulation of particles on the liquid surface may result in an increase of the surface tension (Belden and Techet 2011).

The class of projection techniques contains a wide variety of measurement principles ranging from one-dimensional to three-dimensional techniques. In the one- and two-dimensional measurements a laser beam or light sheet is projected on a liquid surface, where the water is either doped with a fluorescent dye (Buckley et al 2017) or contains suspended particles (Gomit et al 2015). The resulting absorption or diffusion of the light can then be detected, where the location of the free surface is triangulated using a stereo camera system. The formation of reflection or focusing beamlets and the optical configuration determine the signal to noise ratio and required processing steps (Andre and Bardet 2014). Three-dimensional measurements can be

performed when, either the dye or the particles, absorb or diffuse the incoming light in the near vicinity of the liquid free surface (Tsubaki and Fujita 2005). However, the amount of dye or particles required is substantial and will have an influence on the surface tension. Furthermore, tests in large-scale facilities would produce considerable amounts of contaminated water. Quasi three-dimensional measurement can be obtained by applying a scanning methodology (Brücker 1997; Gomit et al 2015).

Methods based on the properties of light, such as reflection or refraction, are also numerous in their application and implementation, e.g. (Gomit et al 2013; Moisy et al 2009; Savelsberg et al 2006). In these applications either, the refraction or reflection of, a single laser beam is tracked (Savelsberg et al 2006) or a reference pattern is imaged (Gomit et al 2013; Moisy et al 2009). The methods based on the properties of light are, often, limited to weak deformations, weak slopes, small surface-pattern distances and small paraxial angles (Moisy et al 2009).

In this work a measurement technique is presented that is intended for future experimental work on wave impacts as part of the public-private research programme Sloshing of Liquefied Natural Gas (SLING). The newly developed experimental set-up imposes optical (single view) and physical restrictions (wave flume enclosed in an autoclave) that complicate the measurement (to be presented, Bogaert et al 2018; Bogaert et al 2018). Based on the presented overview of surface measurement techniques, it can be concluded that a combination of several measurement principles is necessary to obtain measurements over an intended domain of $100 \times 100 \times 100$ mm^3 with a target accuracy of 1 mm. The accuracy of the technique will be evaluated using a conventional side-view measurement (Buckley et al 2017; Wang et al 2018).

3. Experimental set-up

The measurement technique is a combination of planar laser-induced fluorescence (PLIF) with a stereo camera system and a scanning approach to obtain quasi three-dimensional measurements. In principal a single camera would suffice as the light sheet fixes the Z-location and the surface shape can be represented by a segment with varying (X, Y)-coordinates based on a local mapping function. However, in the intended application three-dimensional surface deformations may block one of the viewing directions. If unobstructed, both cameras should yield the same surface shape, allowing a reduction in the measurement uncertainty. Furthermore, to obtain accurate measurements perfect alignment between the calibration plate and the light sheet is required (Wieneke 2005). Consequently, the stereo camera system is used to increase the accuracy of the

measurements, to minimize errors due to refractive index changes and to relax the alignment constraint.

The scanning stereo camera system is calibrated using a multistep calibration procedure similar to the self-calibration procedure used in stereo-PIV (Wieneke 2005). To obtain sufficient information to perform a self-calibration procedure, the domain is sampled by imaging several still water heights.

An initial inverse polynomial mapping function $\boldsymbol{F}_{\boldsymbol{i,j}}^{-1}(\bar{x})$, with cubic dependence on x and y, is determined by placing a planar calibration target at two distinct Z_j-locations that encompass the domain to be calibrated, where the subscript indices i and j are, respectively, the camera and Z_j-location (Soloff et al 1997). The inverse mapping function maps image coordinates $[\bar{x}_k = (x_k, y_k)]$ to world coordinates $[\bar{X}_k = (X_k, Y_k, Z_k)]$. Data in the image plane is backprojected to a Z_j-location and it is assumed that $Z_k = 0$. The backprojected data is, after determining the inverse mapping function, assumed to be at a uniform Z_j-location (Adrian and Westerweel 2011).

The self-calibration procedure is performed for each light sheet location, indicated by a subscript n. At each of the defined free surface resting heights and per light sheet location, image coordinates are backprojected and world coordinates are triangulated. The image (x_n, y_n) and triangulated world coordinates (X_n, Y_n) are used to determine a third order inverse polynomial mapping function $\bar{X}_{\boldsymbol{n}}(X_n, Y_n, 0) = \boldsymbol{F}_{\boldsymbol{i,n}}^{-\boldsymbol{1}}(\bar{x}_n)$ at location n and for camera i. The Z_n-coordinates are determined by fitting a cubic polynomial surface in X_n and Y_n to the world coordinates, resulting in a mapping according to $Z_n = \widetilde{\boldsymbol{F}}_n(X_n, Y_n)$. After the self-calibration procedure, the coordinate origins and directions must be determined. For the X- and Z-coordinate these are imposed by the initial inverse polynomial mapping function, whereas the Y-coordinate origin is redefined by fitting a polynomial function to the determined free surface location at rest for all the light sheet locations. A flow chart of the self-calibration procedure is depicted in Fig. 1.

The performance of the experimental set-up is evaluated in the water tunnel of the Laboratory for Aero- and Hydrodynamics at the Delft University of Technology. The test section has a cross section of 0.6×0.6 m^2 with a length of 5 m, wherein the boundary-layer is controlled with a false bottom that is placed 190 mm above the original bottom. In the resulting open-channel flow a bump geometry is placed, with which conditions can be obtained ranging from a stationary wave to a hydraulic jump (Gui et al 2014). The free surface flow is defined by the upstream Froude number $Fr = U/\sqrt{gH}$, the bump height $H_b = 119$ mm and the bump length $L = 2.5H_b$.

The obtained free surface flow is repeatable and of increasingly complex shape, which facilitates the characterization of the measurement technique before applying it to the target application of impacting waves.

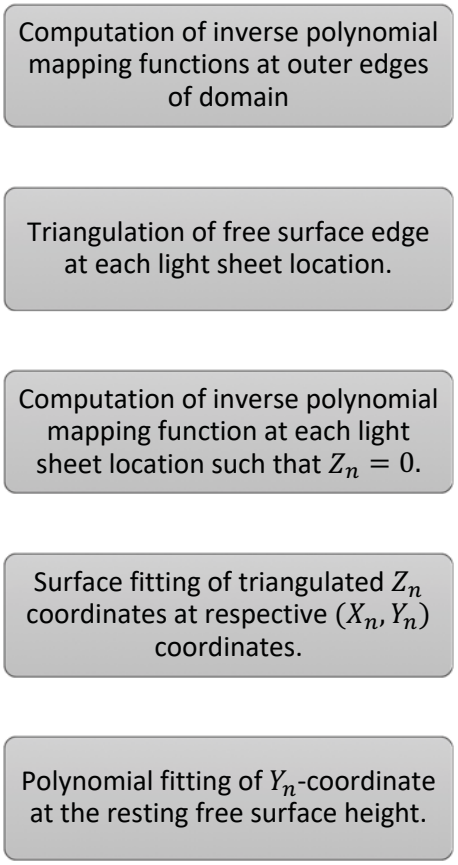

Fig. 1 Flow chart of the self-calibration procedure.

The stereo images were acquired using two high-resolution CCD cameras (LaVision Imager LX 16M). Initially the high-resolution and low-speed stereo-cameras are used to evaluate the performance of the measurement technique. In future applications the low-speed stereo-cameras will be replaced by high-speed cameras. The stereo-camera system used a small lens aperture (f-stop of 22) and the camera lenses (NIKON MIRCRO-NIKOR, 105 mm) were equipped with long pass filters (Schott OG570), such that only the emitted fluorescent light was imaged. The reference (side-view) images were acquired using a single CCD camera (LaVision Imager Intense) at a medium lens aperture (f-stop of 8) and the camera lens (NIKON MICRO-NIKOR, 35 mm) was equipped with the same long pass filter (Schott OG570). Rhodamine WT dye (excitation at 530 nm and emission 555 nm) is added to the liquid in a concentration of 120 mg/m^3, which is excited using a light sheet generated by a twin-cavity double-pulsed

Nd:YAG laser (Spectra-physics Quanta Ray, 200 mJ/pulse, $1-2$ ns pulse duration, 532 nm wavelength).

As depicted in figure 1 the stereo cameras were placed at an angle $\alpha = 15$ deg with respect to the Y-axis, a baseline distance of $B = 500$ mm between the two camera centers, and a vertical distance $Z = 1000$ mm from the center to the bottom. The reference camera was placed at an angle $\beta = 15$ deg with respect to the Z-axis, a horizontal distance of $D = 800$ mm from the channel center line, and a vertical distance $Z_c = 200$ mm from the center to the second bottom.

The reference camera has a magnification $M_0 = 0.05$ and a depth of field $\delta_z \approx 90$ mm. On the other hand, the stereo-cameras have a variable magnification over their field of view due to the small angle with respect to the Y-axis. An estimate of the magnification at the center plane is $M_0 = 0.14$, with a depth of field of $\delta_z \approx 83$ mm. The variation in averaged magnification over the Y-coordinate, expressed in micrometers per pixel, is substantial between the Z_j-locations that encompass the domain. However, the variation between the two cameras for, respectively, their positive and negative Z_j-locations with respect to the center plane is minimal. The averaged magnification over the Y-coordinate varies between approximately 180 and 250 μm/pixel over the domain, whereas the X-coordinate remains relatively similar at approximately 55 μm/pixel.

The laser beam is directed by several mirrors so that it enters the (unperturbed) liquid free surface from above aligned with the Y-axis. The light sheet is scanned over the domain in the spanwise (Z) direction using the mirror that aligns the laser sheet with the Y-axis. Scanning of the domain is achieved using a galvanometer (Cambridge Technology 6210H), which scanned the laser beam over a cylindrical lens with focal length of -12.5 mm creating a light sheet that was large enough for the current field of view. The beam size in front of the scanning mirror had to be reduced, using a Galilean telescope with focal lengths of 150 and -50 mm resulting in a magnification of 1/3, to utilize the small diameter mirror (5 mm) attached to the galvanometer.

The edge of the liquid free surface has to be determined for the self-calibration and measurement procedures. However, edge detection is a non-trivial procedure and there is a large variety in methods that are, often, tailored to specific applications. Intensity variations over the liquid free surface result in localized and large intensity gradients, which limit the use of Sobel or Canny edge detection algorithms (André and Bardet 2014). To minimize the influence of these localized effects a multi-step approach is applied.

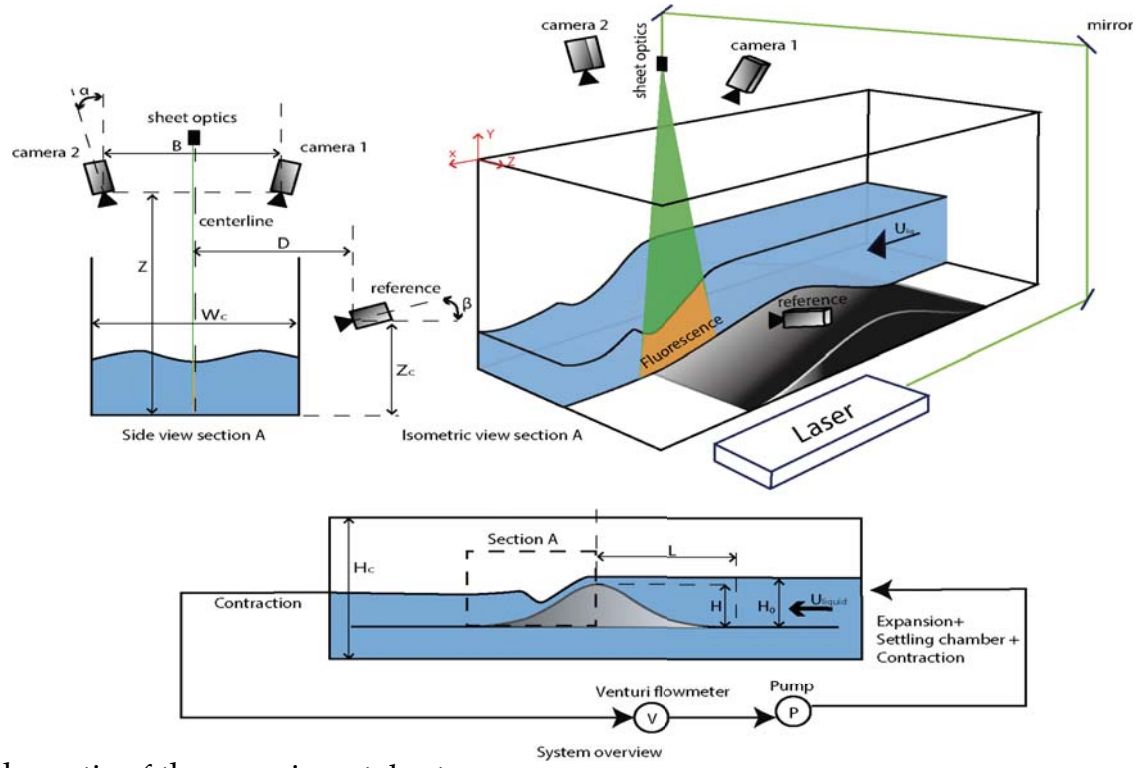

Fig. 2 Schematic of the experimental set-up.

The image is smoothed with a median filter which removes isolated pixels while maintaining the spatial resolution (Jain 1989). Then overlapping sliding windows are applied in the x-direction where for each sliding window a local threshold level is determined using a single step Otsu's method (Otsu 1979). Errors, due to large intensity variations, are minimized by averaging the local threshold over adjacent windows. In the third step morphological operations are applied (erosion, removal and dilation), which result in the removal of small, erroneously, detected elements (Adrian & Westerweel 2011). The last step applies a multi-level local thresholding at places where the pixel to pixel variation of the detected free surface is larger than a set threshold to correct for large local intensity variations. The detected edge is filtered using a Hampel filter to remove local outliers and smoothed using a moving average filter. A result of the edge detection operation is shown in Fig. 3.

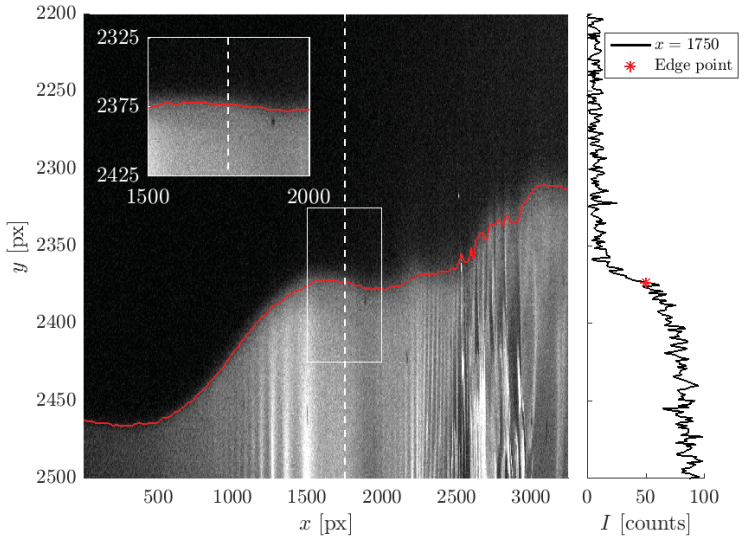

Fig. 3 Image of camera 1 with the detected edge shown in red. The inset shows a zoom of the detected edge at the location of the white rectangle. The right inset displays the intensity values over the white-dotted line, where the detected edge is shown with the red (∗).

5. Results and discussion

Experiments were performed in the water tunnel with an initial still water height of 144 mm were the light sheet scanned $n = 45$ planes, in a saw tooth profile, over a domain of approximately $Z = 70$ mm with an inter plane distance of $\Delta Z \approx 1.5$ mm. The recording rate of the cameras was limited to $f_r = 1.44$ Hz, so one saw tooth profile was scanned in $t_r = 31.25$ s.

The low-speed camera system is, currently, not able to resolve the fluctuations of the liquid free surface. Therefore, time-averaging is applied over $N_n = 100$ images per light sheet location. The time-averaging increases the signal to noise ratio, which has a positive effect on the robustness of the edge processing. The initial water level is indicated by case 0. The water tunnel was operated at three different Froude numbers, that are indicated by case 1 ($Fr = 0.12 \pm 8.9 \times 10^{-3}$), case 2 ($Fr = 0.15 \pm 17 \times 10^{-3}$), case 3 ($Fr = 0.20 \pm 15 \times 10^{-3}$).

The accuracy of the self-calibration procedure is evaluated using Fig. 4, where the still water heights determined with the stereo-camera system (Y_m) are plotted with respect to the reference camera (Y_{ref}). The overall agreement between reference camera and stereo-camera system is visualized with a linear line. Furthermore, the absolute difference between the reference and stereo-camera system is shown in the inset. The difference that is observed between the stereo-cameras over the scanned planes is minimal, but there is a significant difference between the reference and stereo-camera system. These differences might be introduced by several sources of error, e.g. a limitation of the technique, timing and/or read-out errors or edge detection errors.

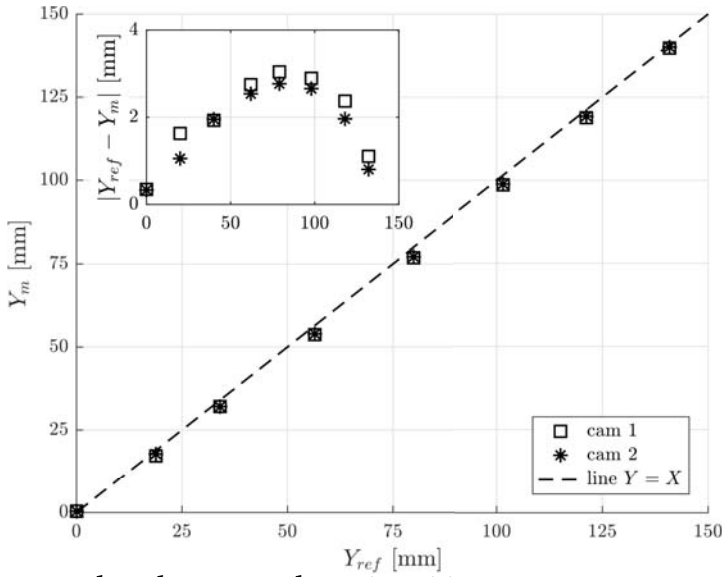

Fig. 4 Reproduced still water heights from the self-calibration procedure. The reference camera is indicated by Y_{ref} and the measured locations are indacted by Y_m.

The time averaged free surface profiles obtained at the measured range of Froude numbers, for the reference camera and stereo-camera 1, are shown in Fig.5. Due to the systematic error that is observed between the stereo-cameras and the reference camera only the data of a single stereo-camera is plotted in Fig. 5. The averaged systematic error, per measurement case, is determined over the measurement data that has been interpolated to the coarser grid of the reference camera and is depicted in the inset of Fig. 5. The trend and order of magnitude of the averaged systematic error for both stereo-cameras is comparable to the error of the self-calibration procedure. The systematic error is, on average, 2.7 ± 1.2 mm, which implies an average pixel value difference of 11 ± 5 pixels. As the error is systematic and the order of magnitude is comparable for both stereo-cameras, it seems to imply that the edge detection procedure is not robust enough. The deviation is not unexpected, as the edge detection procedure determines the location based on a single threshold value, as shown on the inset of Fig.3, where the location is already arguable. The edge detection procedure can be improved by utilizing the Gaussian beam characteristics as the integral over the intensity profile is an error-function. However, the terms and charactersitcs of this error-function, for the current stereo-camera system, have not yet been determined.

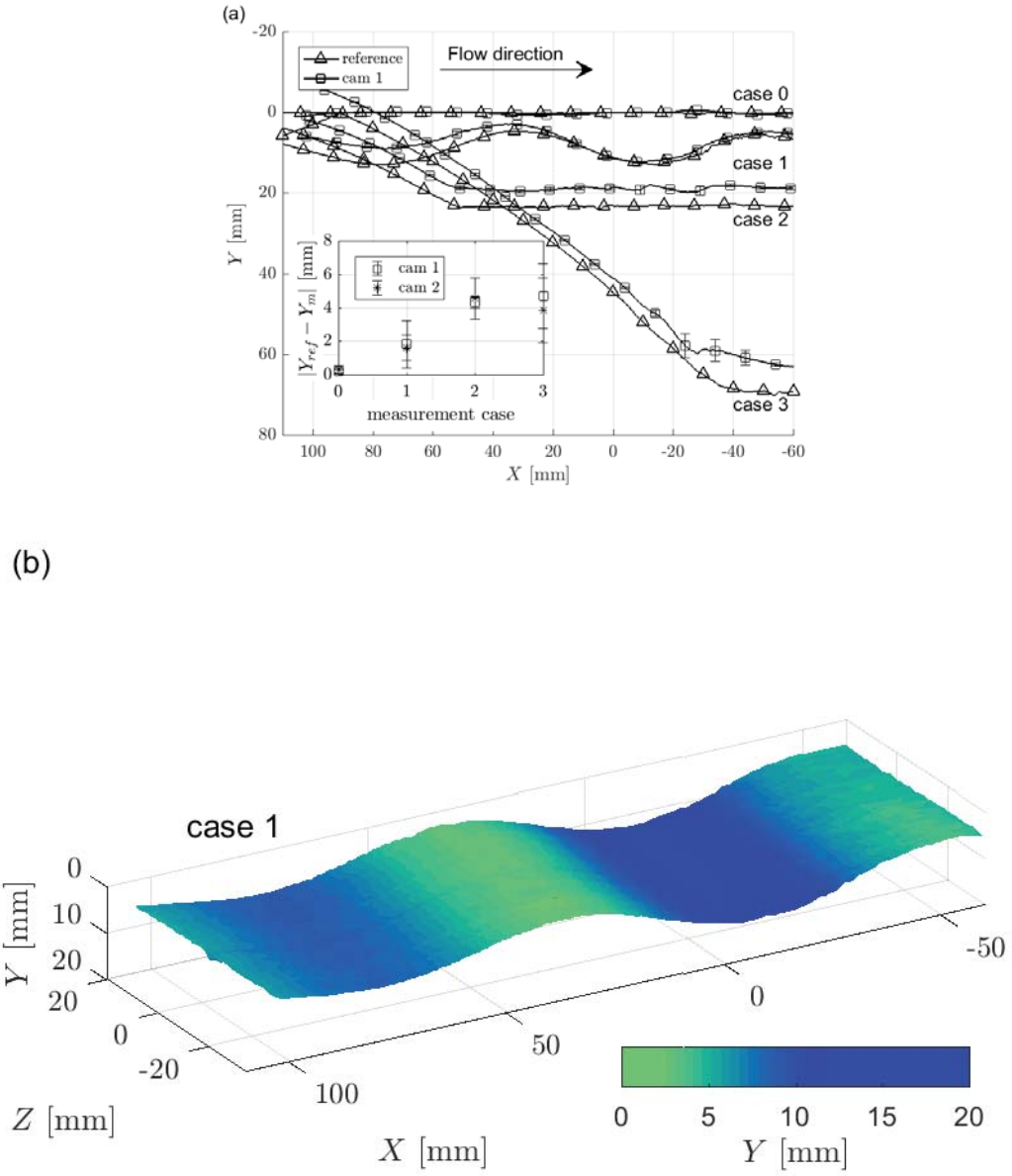

Fig. 5 (a) Reconstructed free surface profiles for the reference camera and stereo-camera 1, where the flow direction is from positive to negative X. The different free surface profiles are obtained at the selected Froude numbers, indicated by their respective case numbers. The error bars on the stereo-camera measurements are of the order of the marker size. The inset shows the absolute averaged difference, including one standard deviation error bars, of the stereo-camera 1 and 2 with respect to the reference measurement. **(b)** Three-dimensional representation of the averaged free surface profile for case 1.

6. Conclusion

We devised a measurement system capable of characterizing the free surface profile over a domain of $(X, Y, Z) = (170, 100, 62)$ mm, with an averaged systematic error of 2.7 ± 1.2 mm. The stereo-camera system relaxes the alignment constraints of a standard planar measurement technique by employing a self-calibration procedure. The systematic error that is observed, with both the self-calibration and measurement data, implies that the current edge detection procedure is not robust.

In future work we will focus on three aspects of the measurement system, namely the robustness of the edge detection procedure and the measurement frequency. The later can be improved by employing high-speed equipment, such as high-speed cameras and lasers, and by employing a dual-exposure technique that allows us to stack multiple profiles in a single image. The robustness of the system can be improved by utilizing the Gaussina beam charactersitics and overall by increasing the signal to noise ratio. This will also imrove the accuracy of the system and processing, which will be evaluated at a later moment.

Acknowledgements

This work is part of the public-private research programme Sloshing of Liquefied Natural Gas (SLING). The support by the Netherlands Organisation for Scientific Research (NWO) Domain Applied and Engineering Sciences, and project partners is gratefully acknowledged.

References

Adrian, R. J., & Westerweel, J. (2011). *Particle image velocimetry* (No. 30). Cambridge University Press.

André, M. A., & Bardet, P. M. (2014). Velocity field, surface profile and curvature resolution of steep and short free-surface waves. *Experiments in fluids*, *55*(4), 1709.

Bagnold, R. A. (1939). Interim report on wave-pressure research. *Journal of the Institution of Civil Engineers*, *12*(7), 202-226.

Belden, J., & Techet, A. H. (2011). Simultaneous quantitative flow measurement using PIV on both sides of the air–water interface for breaking waves. *Experiments in Fluids*, *50*(1), 149-161.

Blackmore, P. A., & Hewson, P. J. (1984). Experiments on full-scale wave impact pressures. *Coastal Engineering*, *8*(4), 331-346.

Bredmose, H., Bullock, G. N., & Hogg, A. J. (2015). Violent breaking wave impacts. Part 3. Effects of scale and aeration. *Journal of Fluid Mechanics*, *765*, 82-113.

Bogaert, H., Brosset, L., Kaminski, M., Koren, B., van der Meer, D., Poelma, C., Sanderse, B., Veldman, A., & Westerweel, J. (2018). SLING research programme: Exploring the last frontier of sloshing physics. *ISOPE proceedings 2018*.

Bogaert, H., Novakovic, V., Fernandes, A. (2018). Multiphase Wave lab developed by SLING programme. *ISOPE proceedings 2018*.

Brücker, C. (1997). 3D scanning PIV applied to an air flow in a motored engine using digital high-speed video. *Measurement Science and Technology*, *8*(12), 1480.

Buckley, M. P., & Veron, F. (2017). Airflow measurements at a wavy air–water interface using PIV and LIF. *Experiments in Fluids*, *58*(11), 161.

Bullock, G. N., Obhrai, C., Peregrine, D. H., & Bredmose, H. (2007). Violent breaking wave impacts. Part 1: Results from large-scale regular wave tests on vertical and sloping walls. *Coastal Engineering*, *54*(8), 602-617.

Chan, E. S., & Melville, W. K. (1988). Deep-water plunging wave pressures on a vertical plane wall. *Proc. R. Soc. Lond. A*, *417*(1852), 95-131.

Gomit, G., Chatellier, L., Calluaud, D., David, L., Fréchou, D., Boucheron, R., ... & Hubert, C. (2015). Large-scale free surface measurement for the analysis of ship waves in a towing tank. *Experiments in Fluids*, *56*(10), 184.

Gomit, G., Chatellier, L., Calluaud, D., & David, L. (2013). Free surface measurement by stereo-refraction. *Experiments in fluids*, *54*(6), 1540.

Gui, L., Yoon, H., & Stern, F. (2014). Techniques for measuring bulge–scar pattern of free surface deformation and related velocity distribution in shallow water flow over a bump. *Experiments in fluids*, *55*(4), 1721.

Jain, A. K. (1989). *Fundamentals of digital image processing*. Englewood Cliffs, NJ: Prentice Hall,.

Lugni, C., Brocchini, M., & Faltinsen, O. M. (2010). Evolution of the air cavity during a depressurized wave impact. II. The dynamic field. *Physics of fluids*, *22*(5), 056102.

Lugni, C., Miozzi, M., Brocchini, M., & Faltinsen, O. M. (2010). Evolution of the air cavity during a depressurized wave impact. I. The kinematic flow field. *Physics of fluids*, *22*(22), 056101.

Moisy, F., Rabaud, M., & Salsac, K. (2009). A synthetic Schlieren method for the measurement of the topography of a liquid interface. *Experiments in Fluids*, *46*(6), 1021.

Otsu, N. (1979). A threshold selection method from gray-level histograms. *IEEE transactions on systems, man, and cybernetics*, *9*(1), 62-66.

Peregrine, D. H. (2003). Water-wave impact on walls. *Annual review of fluid mechanics*, *35*(1), 23-43.

Savelsberg, R., Holten, A., & van de Water, W. (2006). Measurement of the gradient field of a turbulent free surface. *Experiments in fluids*, *41*(4), 629-640.

Soloff, S. M., Adrian, R. J., & Liu, Z. C. (1997). Distortion compensation for generalized stereoscopic particle image velocimetry. *Measurement science and technology*, *8*(12), 1441.

Song, Y. K., Chang, K. A., Ryu, Y., & Kwon, S. H. (2013). Experimental study on flow kinematics and impact pressure in liquid sloshing. *Experiments in fluids*, *54*(9), 1592.

Turney, D. E., Anderer, A., & Banerjee, S. (2009). A method for three-dimensional interfacial particle image velocimetry (3D-IPIV) of an air–water interface. *Measurement Science and Technology*, *20*(4), 045403.

Wanek, J. M., & Wu, C. H. (2006). Automated trinocular stereo imaging system for three-dimensional surface wave measurements. *Ocean engineering*, *33*(5-6), 723-747.

Wang, A., Ikeda-Gilbert, C. M., Duncan, J. H., Lathrop, D. P., Cooker, M. J., & Fullerton, A. M. (2018). The impact of a deep-water plunging breaker on a wall with its bottom edge close to the mean water surface. *Journal of Fluid Mechanics*, *843*, 680-721.

Wieneke, B. (2005). Stereo-PIV using self-calibration on particle images. *Experiments in fluids*, *39*(2), 267-280.

Zavadsky, A., Benetazzo, A., & Shemer, L. (2017). On the two-dimensional structure of short gravity waves in a wind wave tank. *Physics of Fluids*, *29*(1), 016601.